nature nanotechnology

Article

https://doi.org/10.1038/s41565-023-01394-3

Hierarchical helical carbon nanotube fibre as a bone-integrating anterior cruciate ligament replacement

In the format provided by the authors and unedited

This PDF file includes:

Supplementary Notes 1 to 9 (Pages S2-S6)
Supplementary Figures 1 to 24 (Pages S7-S30)
Supplementary Tables 1 and 2 (Page S31 and S32)
Captions for Supplementary Movies 1 to 4 (Page S33)
Captions for Supplementary Data 1 to 7 (Page S33)
Supplementary References (Page S34 and S35)

Supplementary Notes

1. Preparation of CNT fibres

The spinnable CNT arrays were synthesized by chemical vapor deposition. Fe (1 nm)/Al_2O_3 (3 nm) was deposited on a silicon wafer by electron-beam evaporation as the catalyst. The synthesis occurred in a tube furnace with a mixed flowing gas of carbon source of ethylene (90 standard cubic centimeter per minute (sccm)) and carrying gas of Ar (400 sccm) and H_2 (30 sccm). It was performed at 740 °C for 10 minutes. An aligned CNT sheet was directly drawn from the CNT array using a knife and stacked on a glass substrate. CNT fibres were produced by twisting the CNT sheet at a rotary speed of 1000 revolutions per minute and wound on a collecting drum. Some of the primary CNT fibres utilized to produce HHF were prepared by floating chemical vapor deposition. In this method, thiophene (1-2 wt%) and ferrocene (1-2 wt%) were utilized as the catalyst, and flowing ethanol (> 97 wt%), Ar (200 sccm) and H_2 (2000 sccm) were utilized as carbon source, carrier gas and reduction gas, respectively. CNT aerogel was produced continuously at the hot zone of a tube furnace with the reaction temperature of 1200 °C, and it was then collected into cylindrical hollow socks. The CNT sock was pulled out of the furnace by a titanium rod and then densified through water and ethanol in turn. The CNT sock shrank immediately into CNT ribbon upon arriving at the water surface. It was finally washed by ethanol for further densification, followed by drying, twisting and collecting onto a spool to produce the CNT fibres. The structures of the HHF, CNT fibre, PET fibre and hierarchical helical PET fibres were characterized by scanning electron microscopy (SEM, FE-SEM S-4800, Hitachi, Ltd.) and transmission electron microscopy (TEM, JEM-2100F, JEOL, Ltd.). The photographs were taken by a camera (J1, Nikon, Ltd.).

2. Mechanical performance of CNT fibres

The specific strength of the CNT fibres used to compose our HHF is five times higher than clinical polyester fibre[S1,S2]. These CNT fibres are also much stronger than current commercial fibres, allowing them to lift up to 900,000 times their own weight (**Extended Data Figs. 1b, c**). The mechanical modulus (8 GPa) of these CNT fibres far exceeds that of autogenous ligament (0.2–0.6 GPa) while their failure strain (18%) is comparable to native ligament[S3]. The breaking strengths show these CNT fibres can withstand 1,000,000 cycles of continuous bending as required of an artificial ligament (**Extended Data Fig. 1f**). Such fibres can also be bent, twisted, tied, looped and knitted without any obvious structural damage (**Extended Data Figs. 1g-k**).

3. Mechanical performances of HHFs

A 3.5 cm long HHF was fixed with a stretching formation of 5% using a tensile machine (TA Instruments-Waters LLC ElectroForce 3220). Before bending, deionized water was added into the pool until the fibres were completely immersed. During bending, the HHF was bent with an in-plane type. The MIN condition for such bending refers to the original state before bending (or a curvature radius of ∞), while the MAX condition refers to a curvature radius of 2.34 cm. After 1,000,000 bending cycles, ultraviolet-visible spectra of the water in the pool was measured within the wavelength range of 230–400 nm using a Perkin-Elmer Lambda750. Controls were deionized water and aqueous dispersion solution of CNT with increased concentrations from 1.25×10^{-3} mg/mL to 0.16 mg/mL. To calculate the stiffness and modulus of HHFs, a tensile test was performed according to the standard tensile method to obtain tensile force–displacement curves. The stiffness was calculated as the ratio of tensile force to displacement. The modulus was calculated as the ratio of tensile stress to strain.

The moduli of the HHFs (0.472±0.12 GPa) assembled from CNT fibres were comparable to native ligaments, and the specific strengths (0.587±0.142 N/tex) of the HHF were higher than the majority of grafts including clinical Ligament Advanced Reinforcement System (LARS) grafts and autografts (**Supplementary Table 1**). Moreover, the HHF exhibited similar stiffnesses (79.43±7.46 N/mm) to the LARS grafts and native ligaments[S4,S5] as the formed hierarchical channels inside can effectively accommodate deformations of building CNTs for the desired stiffness.

4. Finite element simulation of CNT fibre

Each CNT fibre consists of bundles of CNTs that are arranged in parallel and are tightly held together by van der Waals forces. Thus, the CNT fibre model is built by parallelly arranging CNTs and spring elements are utilized to represent the van der Waals interaction[S6]. According to current methods[S7], compression is applied to one end of the fibre model to make them bend under the same deformation of 5%. For a CNT fibre model, we defined the void ratio of cross section as the void area over the entire cross-sectional area:

$$\emptyset = \frac{S_v}{S} = \frac{\pi d^2 - n\pi {d_b}^2}{\pi d^2} \qquad (1)$$

where d and d_b represent the diameters of CNT fibre and individual CNT, respectively. The parameter n is the number of CNT bundles in the cross section. For a typical individual CNT, $\emptyset = 0$, $d_b = 7.2$ nm and $n = 1$; for a typical primary CNT fibre, $\emptyset = 0.6$, $d_b = 7.2$ nm, $d = 50$ nm and $n = 19$; for a typical secondary CNT fibre, $\emptyset = 0.6$, $d_b = 50$ nm, $d = 344.6$ nm and $n = 19$. In addition, for a typical individual CNT, the elastic modulus was 1 TPa and Poisson's ratio was 0.3[S8]. Based on these parameters, the von Mises stress (*i.e.*, internal stress) distribution along the fibre model with and without pore structure was simulated using the ABAQUS software.

Finally, the fibre assembled from CNTs with aligned channels showed lower stresses and more uniform stress distributions than individual CNTs (**Supplementary Fig. 3**), which could improve energy dissipation at the graft-to-bone interface to effectively eliminate overload damages of grafts and native bones[S9,S10].

5. Biocompatibility studies of HHF

Biocompatibility studies show that CNT sheet directed an oriented growth of mesenchymal stem cells (MSCs) (**Extended Data Fig. 2a**). No obvious differences in the adhesive area of MSCs were found between the CNT sheets and control glass substrate (**Extended Data Figs. 2a, b**). On HHF, MSCs grew along the helical channels between the primary fibres (**Extended Data Figs. 2c, d**).

When implanted into rabbits for 13 weeks, the histological analysis showed HHF integrated well with the surrounding bone, and the tissue around HHF was similar to that without HHF graft (**Extended Data Figs. 2e, f**). Further enzyme-linked immunosorbent assays (**Extended Data Figs. 2g-j**) showed that the concentrations of alanine aminotransferase and inflammatory cytokines like interleukin-1, tumor-necrosis factor-α and interferon-β all varied within their normal physiological ranges[S11,S12], indicating good biocompatibility at the molecular level.

Long-term safety *in vivo* was further verified by histological analysis of various organs including kidney, cardiac muscle, liver, spleen and lung after HHF implantation of 13 weeks (**Extended Data Fig. 3a**), and no obvious CNT residues were detected in any organ. Masson's trichrome and immunofluorescence staining of these organs showed no obvious collagen deposits or F4/80-positive cells (**Extended Data Fig. 3b**, **c**), further indicating that no CNT fragment accumulation occurred in the organs after HHF implantation. High-resolution

transmission electron microscopy (TEM) images of tissue sections of the organs also did not show obvious CNT fragments (**Supplementary Fig. 4**). Such structural stability of HHF was also verified by the fact that no obvious CNT fragments were detected even after the HHF was repeatedly bent in water for millions of cycles (**Supplementary Fig. 5**). Together, as the building CNTs with lengths of hundreds of micrometers are non-degradable and could not be swallowed by cells, they had been also stably bundled together, the resulting HHF is biocompatible and safe for *in vivo* use.

6. Engineering of cells on fibres

A template PDMS channel with length of 3 mm, width of 1.5 mm and depth of 2 cm was first fabricated *via* soft lithography technique. Individual pieces of carbon plate, helical carbon fibres, HHFs and PET plate, helical PET fibres, hierarchical helical PET fibres were held centrally in the channel to which the MSC gels were then added. For the MSC preparation, MSCs (10^5 cell/mL) were incubated in Dulbecco's modified eagle medium for 3 days at 37 ºC before use. Then MSCs were incubated with trypsin (0.25%, Gibco) for 2 minutes at 37 ºC and pipetted gently to dissociate the cells. After dissociation, the cells were centrifuged (1000 g, 5 min), counted and seeded at 10^6 cells/cm. This ration was maintained for generation of longer cell fibres. Cells were seeded in 1.0 mg/mL rat tail collagen Type I gels (BD Biosciences) and 0.5 mg/mL Matrigel (BD Biosciences, 356234) by pipetting the cell suspension into the PDMS channel. After seeding, the cells were kept in culture for 3 days to allow the collagen matrix to remodel and the cells to grow around the fibre.

7. Immunostaining and fluorescent microscopy

The fibres were fixed in 4% paraformaldehyde for 15 minutes at room temperature. For immunostaining, the samples were permeabilized, blocked for 1 h in 10% fatal bovine serum (Gibco, 10099141) containing 0.2% Tween, and incubated with primary mouse anti-F-actin (1:200, Abcam, ab205) and secondary antigen, Alexa Fluro 488 goat anti-mouse IG (H+L) (1:400, Life Technologies, A11001) and Alexa Fluro 647 goat anti-mouse IG (H+L) (1:400, Life Technologies, A21235) consecutively for 1 hour each at room temperature.

8. Macroscopic evaluation of rabbits after ACL reconstruction

The rabbits were sacrificed from each group at different time points post-operatively. The femur-graft-tibia complex was dissected and the knee joint capsule was exposed for

macroscopic evaluation. The evaluation contains: (1) graft integrity, especially the intra-articular portion; (2) synovial reaction to the graft; (3) carbon deposition; (4) the sign of cartilage degeneration and osteoarthritis; (5) range of motion (ROM) of the knee; (6) Lachman's test and anterior draw test. All images of the knee anatomy were photographed with a digital single lens-reflex camera (5D Mark IV, Canon Inc.) with a macro lens (EF 100 mm 2.8L IS macro, Canon Inc.).

9. Nanometer channels encourage osteointegration

The comparisons of bone repairing between the HHF and carbon fibre suggested nanometer channels of the HHF played an important role for osteointegration and bone regeneration. To verify this, we provided additional control groups with the same material but different structures, i.e., hierarchical helical PET fibres with both nanometer and micrometer channels *vs* helical PET fibre with only micrometer channels. After 4 weeks of implantation in rabbits, the bone tunnels were slightly narrowed for the hierarchically helical PET fibre group, while obvious enlargement occurred for the helical PET fibre group (**Supplementary Fig. 10**). The μCT images showed new bones were formed after implantation of the hierarchical helical PET fibres, while little to no bone was formed around the helical PET fibres. The promoted osteogenesis of nanostructure was also verified by the μCT and pathological results in a rat model (**Supplementary Figs. 11**, **12**).

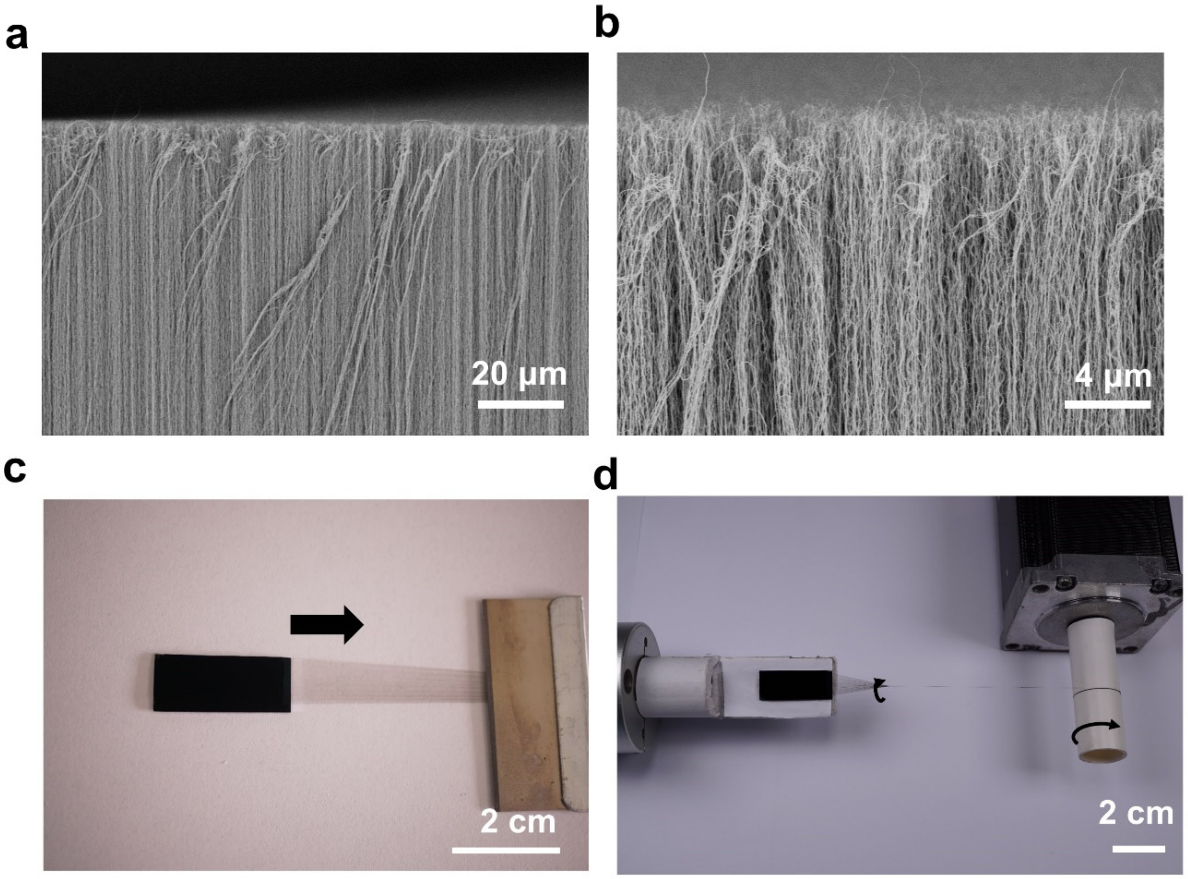

Supplementary Fig. 1 | **a**, **b**, Scanning electron microscopy images of a spinnable carbon nanotube (CNT) array by side view at low and high magnifications, respectively. **c**, Photograph showing the process for drawing out the aligned CNT sheet from a spinnable CNT array. **d**, Photograph showing the preparation of the primary CNT fibre.

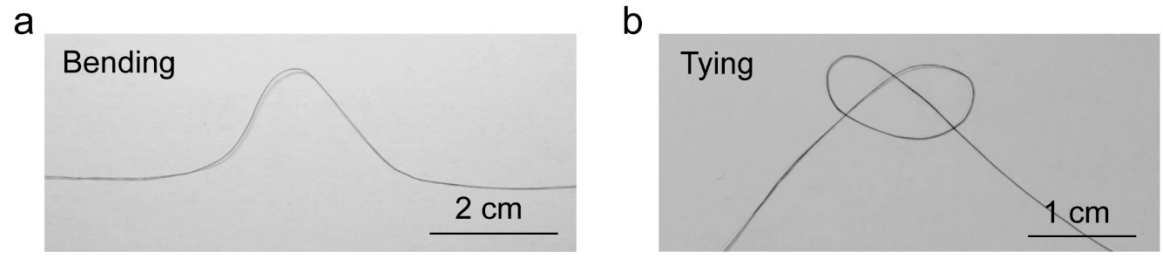

Supplementary Fig. 2 | Photographs showing high flexibility of the CNT fibre under various deformations of bending (**a**) and tying (**b**).

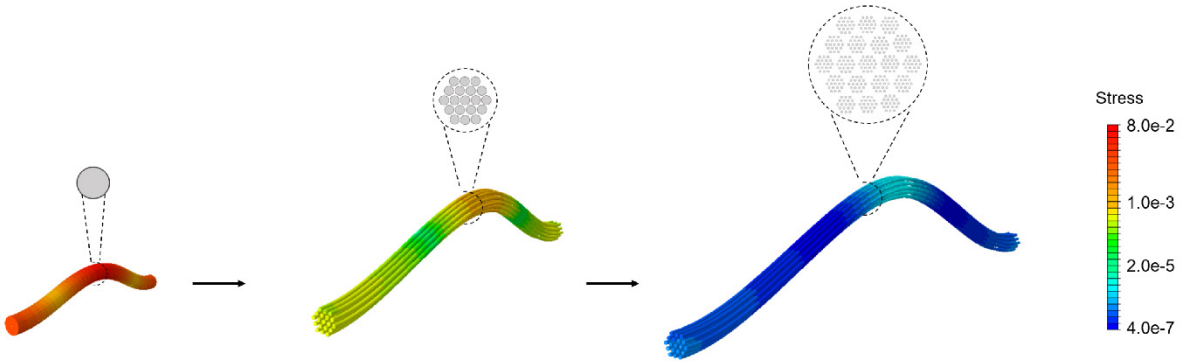

Supplementary Fig. 3 | Finite element simulation of stress distribution of an individual CNT model (left), primary CNT fibre model (middle) and secondary CNT fibre model (right) with hierarchical structure under the same bending deformation of 5%.

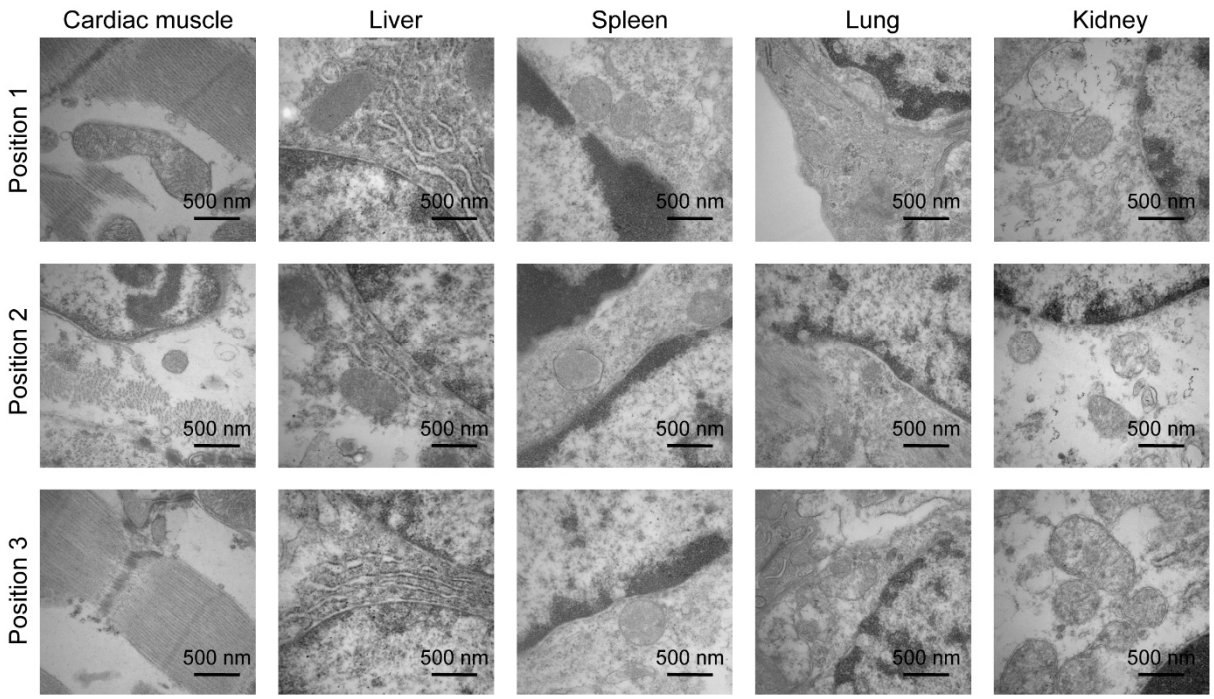

Supplementary Fig. 4 | Transmission electron microscopy images of tissue sections of cardiac muscle, liver, spleen, lung and kidney at 3 different positions after HHF implanted in rabbits for 13 weeks. No CNT fragments are observed in these tissues.

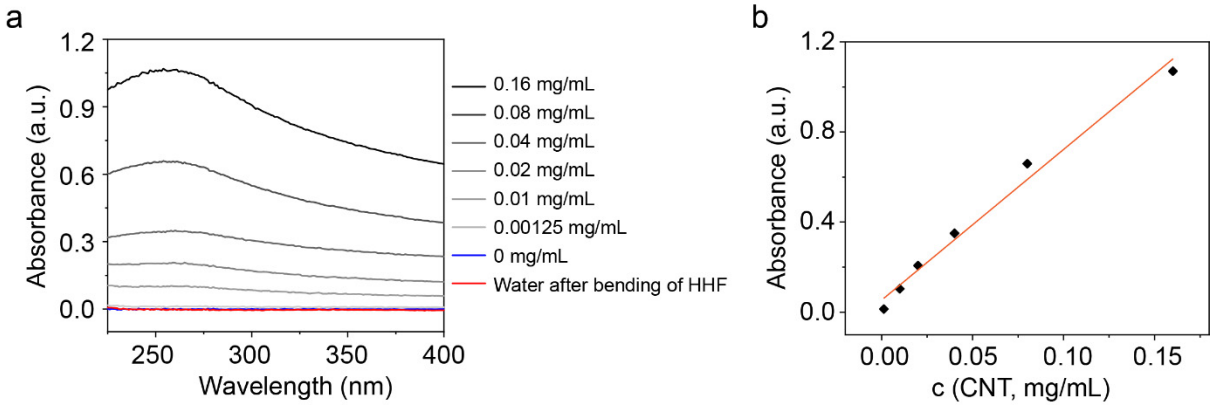

Supplementary Fig. 5 | **a**, Ultraviolet–visible spectra of water in which an HHF have been stretched with a deformation of 5% and then bent for 1,000,000 cycles (red line), deionized water (blue line, control), and several CNT aqueous dispersion with increased concentrations from 1.25×10^{-3} mg/mL to 0.16 mg/mL (black line). CNT aqueous dispersion was prepared by adding commercial CNT powder to deionized water, followed by ultrasonic treatment for 120 min. **b,** Based on the standard curve between the concentrations of CNT aqueous dispersions and absorbance, the water in which HHF has been bent for 1,000,000 cycles shows no CNT fragments.

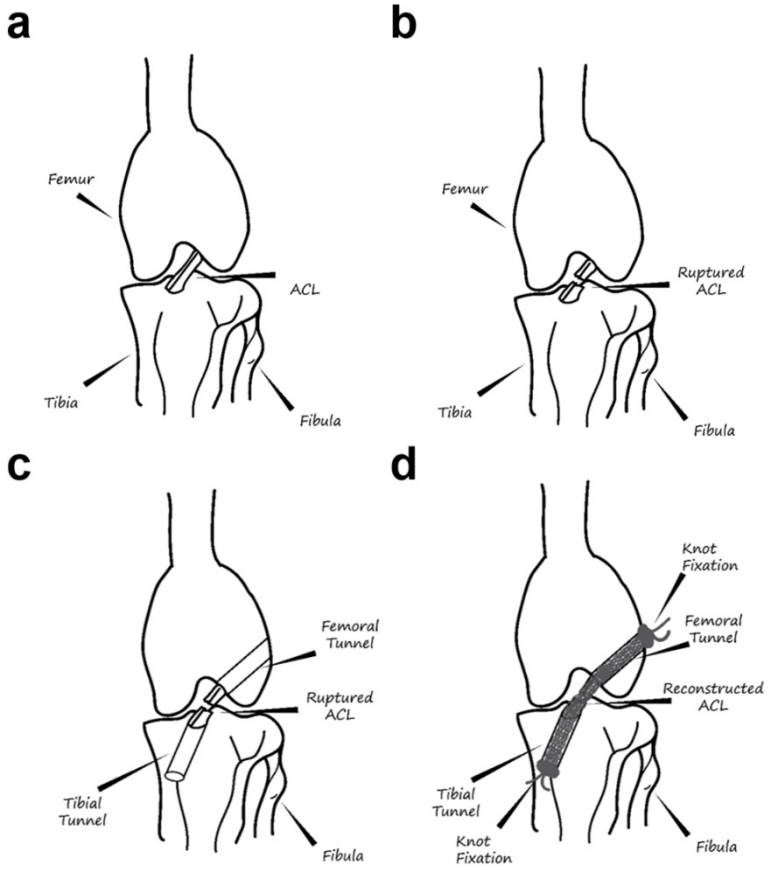

Supplementary Fig. 6 | Schematic demonstration to a typical ACL reconstruction surgery process. a and **b**, The native ACL before and after cutting at the midsubstance by sharp scalpel, respectively. **c**, A Kirschner wire being used to drill the bone tunnel from inside out at the site of the femoral insertion and then behind the tibial insertion of the ACL. **d**, The realization of reconstructed ACL.

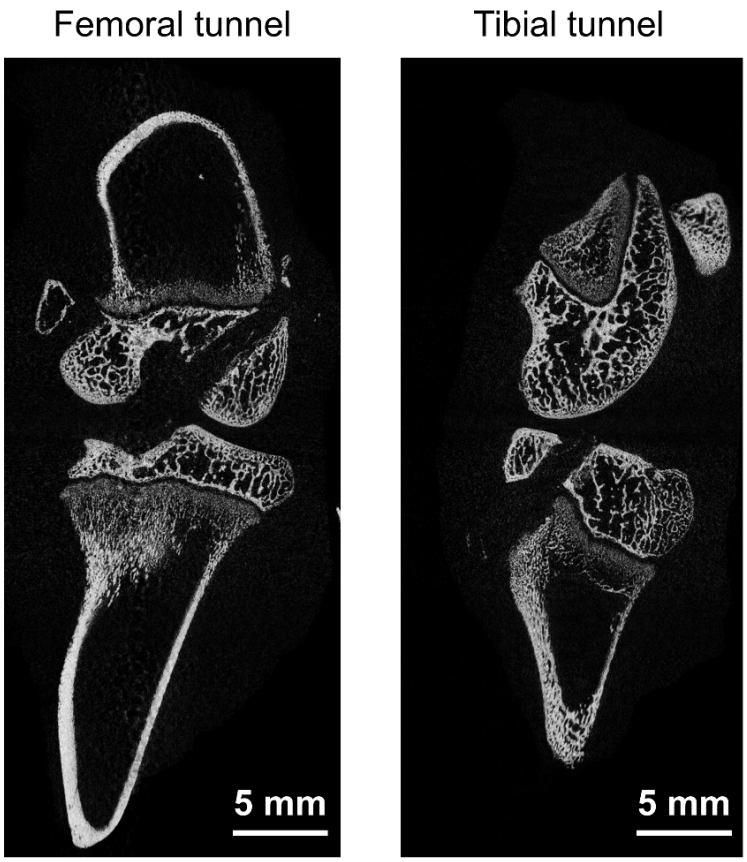

Supplementary Fig. 7 | μCT images of the femur and tibia of rabbits right after ACL reconstruction surgery.

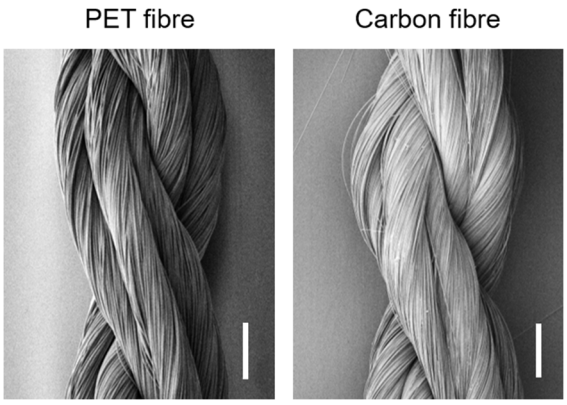

Supplementary Fig. 8 | SEM images of artificial ligaments helically assembled from PET fibres and carbon fibres. Scale bar, 500 μm.

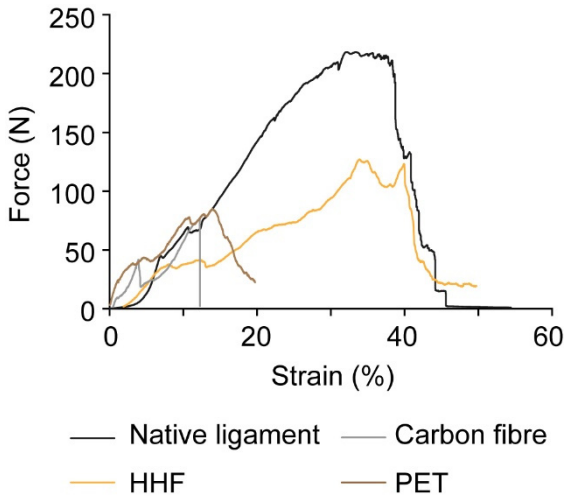

Supplementary Fig. 9 | Force-strain curves of pull-out tests for native ligament, HHF, carbon fibre and PET fibre grafts after implantation for 4 weeks.

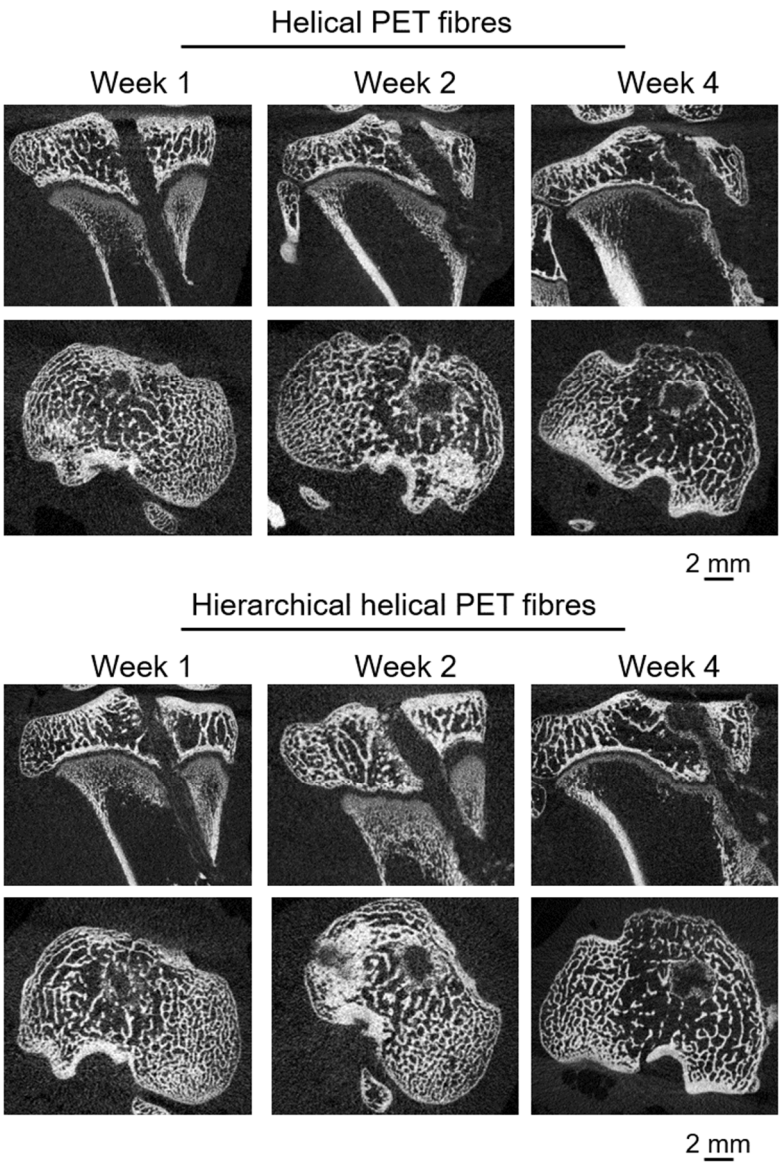

Supplementary Fig. 10 | Typical μCT images of tibial tunnel scanned in a coronal plane (top) and tibial tunnel scanned in an axial plane (bottom) after implantation of helical PET fibres and hierarchical helical PET fibres in rabbits. Images are representative of five experiments.

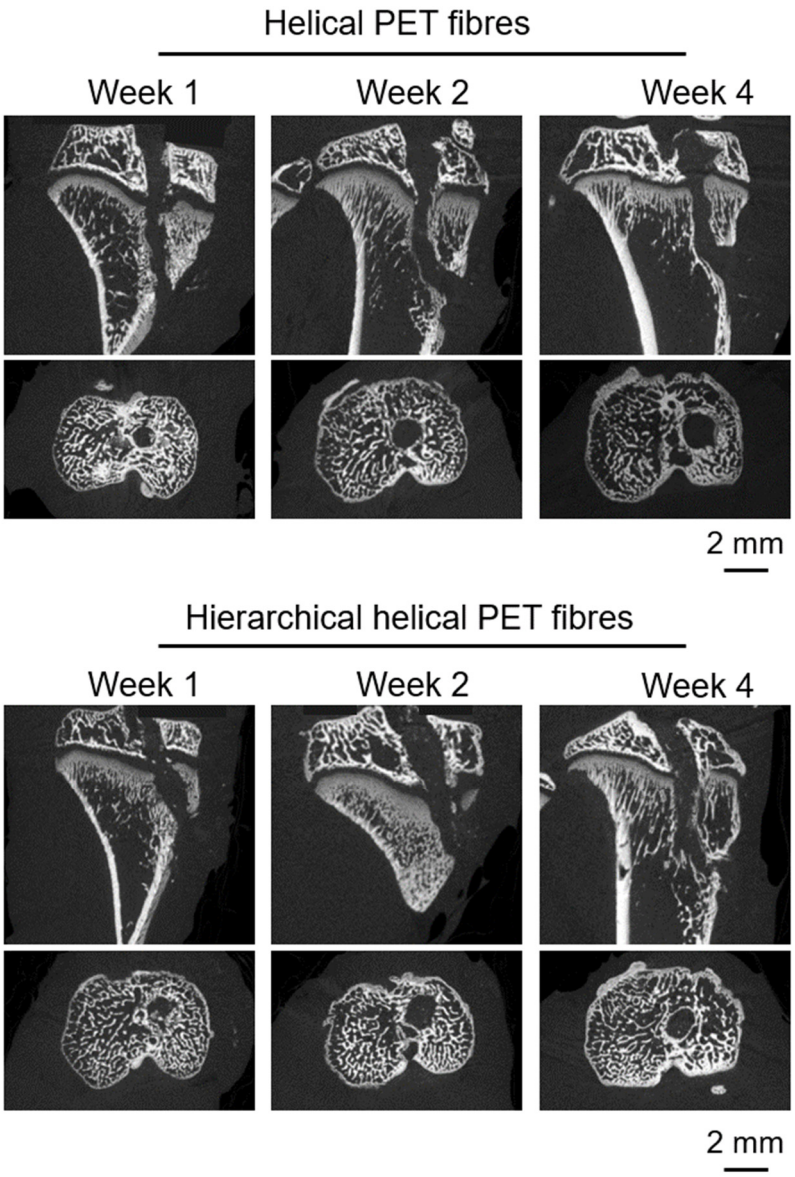

Supplementary Fig. 11 | Typical μCT images of tibial tunnel scanned in a coronal plane (top) and tibial tunnel scanned in an axial plane (bottom) after implantation of helical PET fibres and hierarchical helical PET fibres in rats. Images are representative of five experiments.

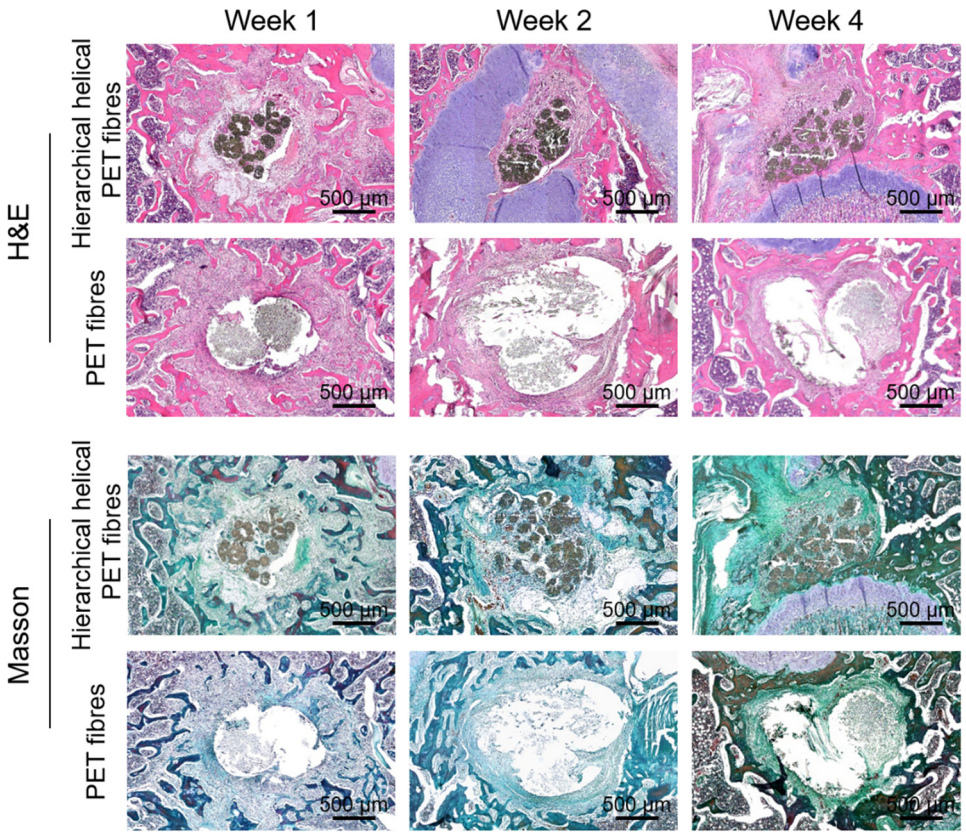

Supplementary Fig. 12 | H&E and Masson-stained images of bone tunnels after implantation of hierarchical helical PET fibre and helical PET fibre in rats. Newly formed bones occupied the bone tunnels and grew into the micrometer channels of hierarchical helical PET fibres.

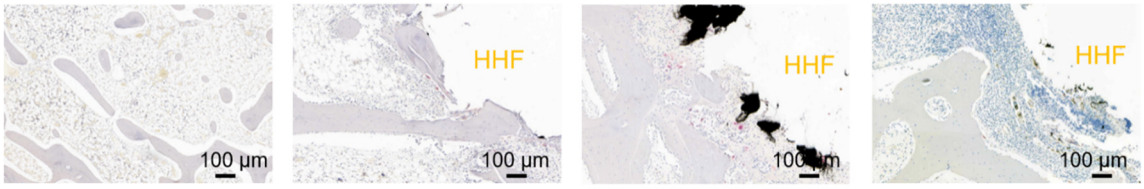

Supplementary Fig. 13 | Tartrate-resistant acid phosphatase (TRAP)-stained slices of bone tunnel after HHF implantation in rabbits. Red: osteoclasts.

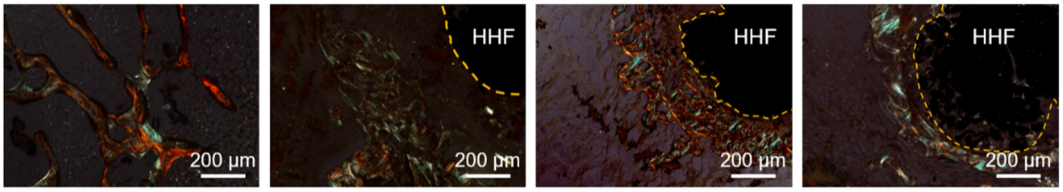

Supplementary Fig. 14 | Picrosirius-red-stained slices of bone tunnel implanted with HHF under polarized light. Collagen tissues are gradually formed at the interfacial region between HHF and host bone from Week 1 to Week 4.

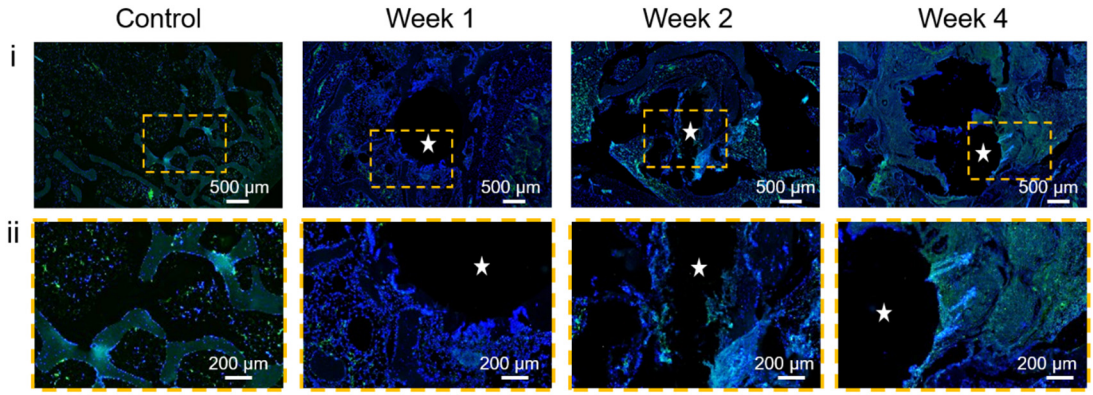

Supplementary Fig. 15 | Immunohistochemical stained images of CD31 expressions after HHF implantation in rabbits. (i) CD31-stained images. Nucleus is stained with DAPI (blue); vessels are stained by both DAPI and anti-CD31 antibodies (blue and green). The position of HHF is marked with white pentalpha. (ii) Magnified view of yellow box in (i) shows CD31-positive vessels are formed at the interface of HHF/native bone.

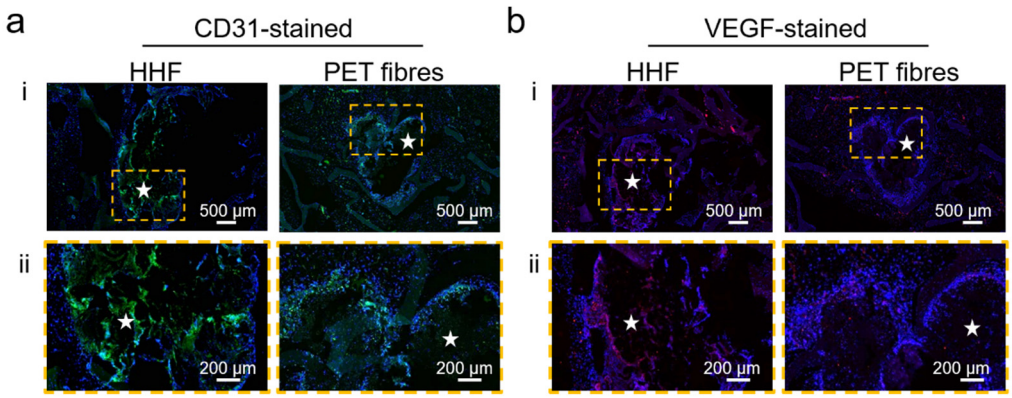

Supplementary Fig. 16 | Immunohistochemical stained images of CD31 and VEGF expressions after implantation of HHF and PET fibres grafts in rabbits for 18 months. a, (i) CD31-stained images. Nucleus is stained with DAPI (blue); vessels are stained by both DAPI and anti-CD31 antibodies (blue and green). The position of HHF and PET fibres is marked with white pentalpha. (ii) Magnified view of yellow box in (i) shows CD31-positive vessels are formed among primary fibres of HHF. **b**, (i) VEGF-stained images. Nucleus is stained with DAPI (blue); vessels are stained by both DAPI and VEGF antibodies (blue and red). The position of HHF and PET fibres is marked with white pentalpha. (ii) Magnified view of yellow box in (i) shows VEGF-positive vessels are formed among primary fibres of HHF.

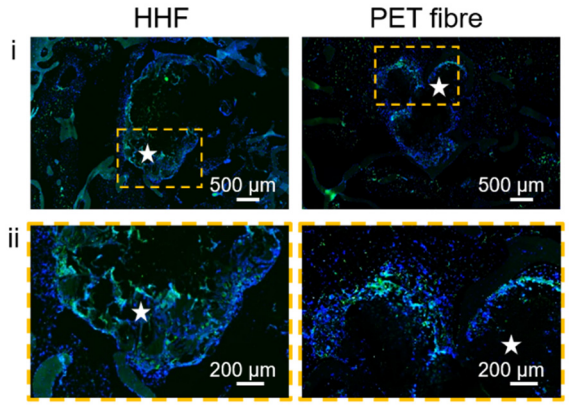

Supplementary Fig. 17 | Immunohistochemical stained images of CGRP expressions after implantation of HHF and PET fibre grafts in rabbits for 18 months. (i) CGRP-stained images. Nucleus is stained with DAPI (blue); nerves are stained by both DAPI and CGRP antibodies (blue and green). The position of HHF and PET fibres is marked with white pentalpha. (ii) Magnified view of yellow box in (i) shows CGRP-positive nerves are formed among primary fibres of HHF.

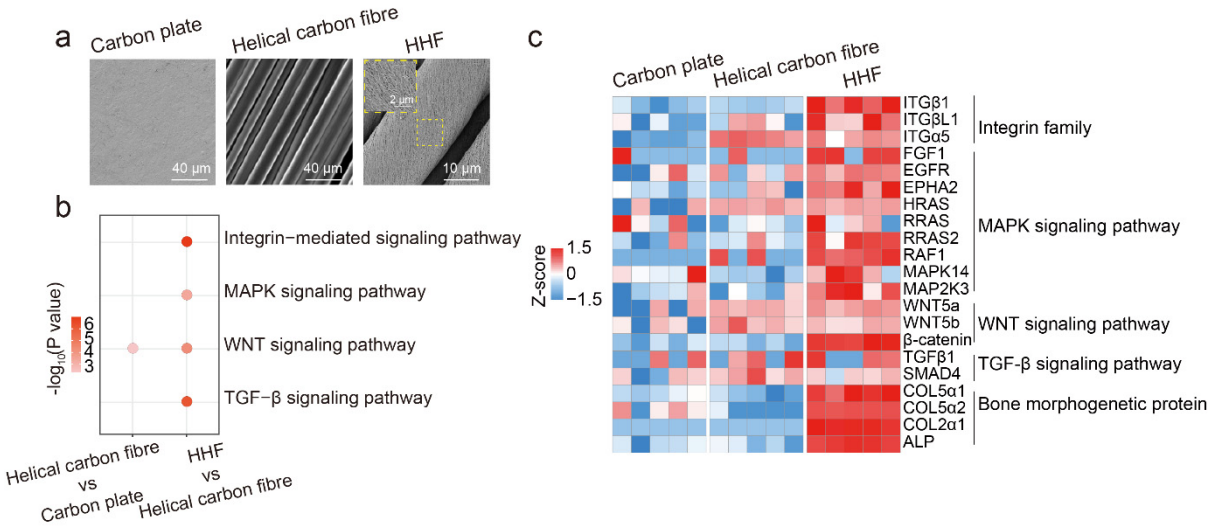

Supplementary Fig. 18 | Proteomic comparisons of osteogenic differentiation of MSCs in carbon plate *vs* helical carbon fibre *vs* HHF on Day 5. a, SEM images of different carbon-based substrates for MSC culturing. Left: carbon plate without nanometer and micrometer channels. Middle: helical carbon fibre with micrometer channels. Right: HHF with both nanometer and micrometer channels. **b**, GO and KEGG enrichment analysis of MSCs based on proteomic dataset showing upregulated osteogenesis-related signaling pathways for different pairwise comparisons (micrometer channel: helical carbon fibre *vs* carbon plate; nanometer channel: HHF *vs* helical carbon fibre). n = 5 biologically independent experiments for each group. Pathway enrichment analysis was performed by DAVID (https://david.ncifcrf.gov/) and ConsensusPathDB (http://cpdb.molgen.mpg.de/CPDB), P value is calculated based on the hypergeometric distribution and the significant pathway (P value < 0.05) was used for further study. **c,** Heatmap analysis of differentially expressed proteins related to osteogenesis of MSCs cultured on carbon plate, helical carbon fibre and HHF. n = 5 biologically independent experiments for each group.

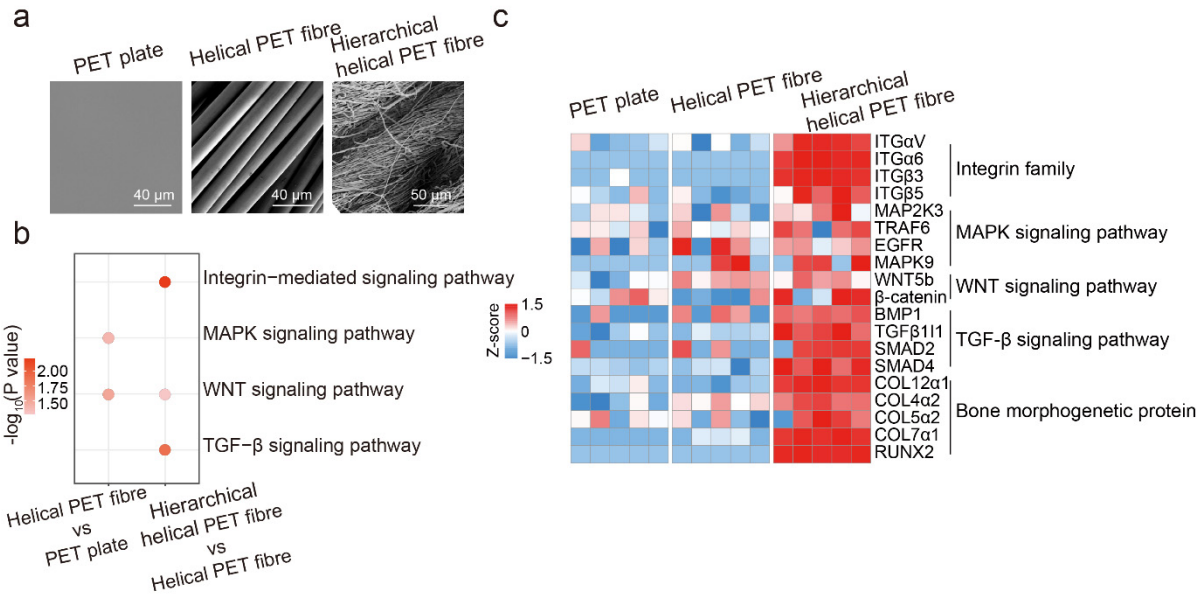

Supplementary Fig. 19 | Proteomic comparisons of osteogenic differentiation of MSCs in PET plate *vs* helical PET fibre *vs* hierarchical helical PET fibre on Day 5. a, SEM images of different PET-based substrates for MSC culturing. Left: PET plate without nanometer and micrometer channels. Middle: helical PET fibre with micrometer channels. Right: hierarchical helical PET fibre with both nanometer and micrometer channels *via* electrospinning method. **b**, GO and KEGG enrichment analysis of MSCs based on proteomic dataset showing upregulated osteogenesis-related signaling pathways for different pairwise comparisons (micrometer channel: helical PET fibre *vs* PET plate; nanometer channel: hierarchical helical PET fibre *vs* helical PET fibre). n = 5 biologically independent experiments for each group. Pathway enrichment analysis was performed by DAVID (https://david.ncifcrf.gov/) and ConsensusPathDB (http://cpdb.molgen.mpg.de/CPDB), P value is calculated based on the hypergeometric distribution and the significant pathway (P value < 0.05) was used for further study. **c,** Heatmap analysis of differentially expressed proteins related to osteogenesis of MSCs cultured on PET plate, helical PET fibre and hierarchical helical PET fibre. n = 5 biologically independent experiments for each group.

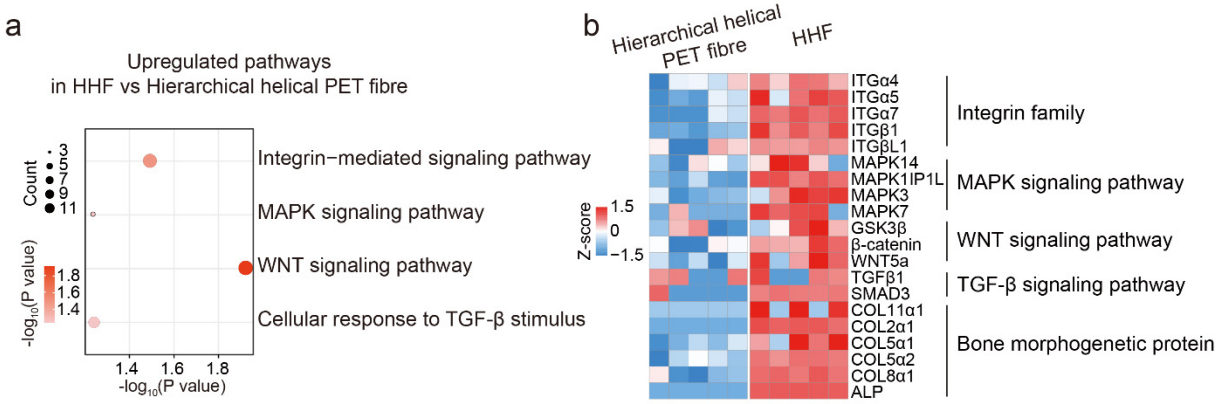

Supplementary Fig. 20 | Proteomic comparison of osteogenic differentiation of MSCs in HHF *vs* hierarchical helical PET fibre on Day 5. a, GO and KEGG enrichment based on proteomic analysis of MSCs cultured on HHF and hierarchical helical PET fibre showing upregulated osteogenesis-related signaling pathways. n = 5 biologically independent experiments for each group. Pathway enrichment analysis was performed by DAVID (https://david.ncifcrf.gov/) and ConsensusPathDB (http://cpdb.molgen.mpg.de/CPDB), P value is calculated based on the hypergeometric distribution and the significant pathway (P value < 0.05) was used for further study. **b**, Heatmap analysis of differentially-expressed proteins related to osteogenesis of MSCs cultured on hierarchical helical PET fibre and HHF. n = 5 biologically independent experiments for each group.

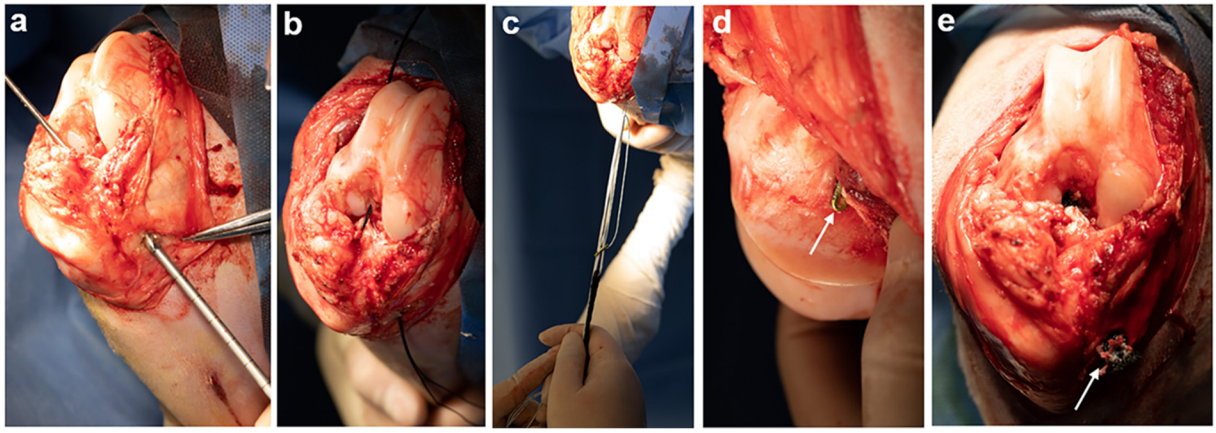

Supplementary Fig. 21 | Typical ACL reconstruction surgery procedure in the sheep model. a, Femoral and tibial tunnel was drilled at the center of ACL anatomical footprint inside-out using a K-wire. The bone tunnel was further dilated into a large diameter of 5.0 mm. **b**, A guiding suture loop was firstly passed through the tibial and femoral tunnel. **c**, The HHF graft was passed through the tunnel. **d**, The graft was fixed on femoral side with adjustable-loop cortical suspension device (marked with the white arrow). **e**, At the tibial side, two ends of HHF graft were tied in to a surgical knot and reinforced with one additional square knot (marked with the white arrow).

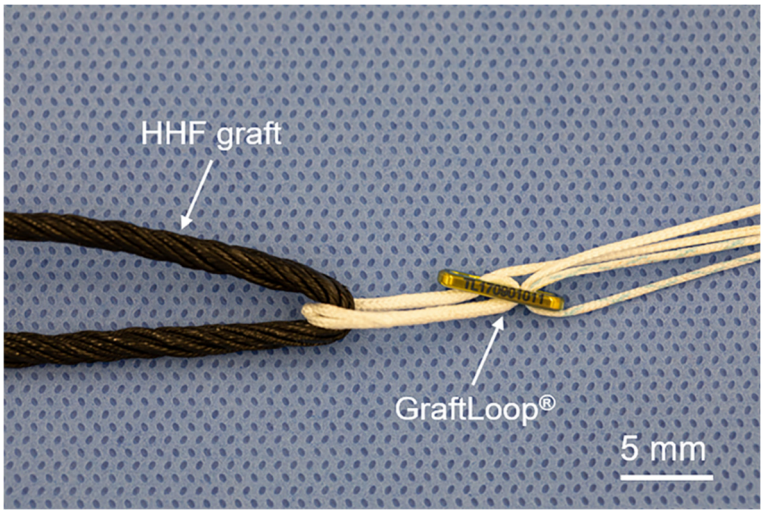

Supplementary Fig. 22 | HHF graft were combined with adjustable-loop cortical suspension device (GraftLoop®, produced by Ligatech Inc, Shanghai) for the ACL reconstruction surgery.

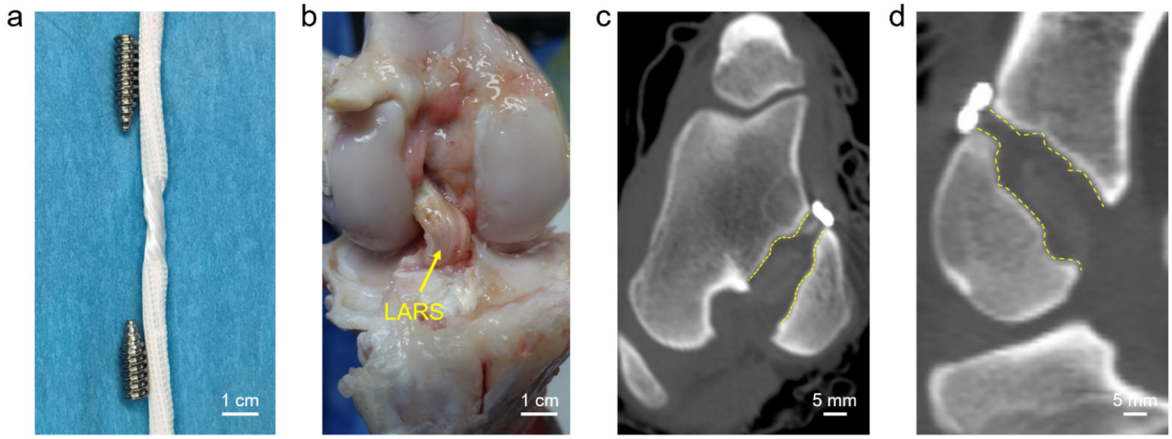

Supplementary Fig. 23 | ACL reconstruction using clinical Ligament Advanced Reinforcement System (LARS) graft in the sheep model. a, Photograph of a commercial LARS graft. **b**, Photograph of the femur-graft-tibia complex specimens of sheep after 3 months of LARS implantation. **c** and **d**, CT images of tibias (in a coronal plane) after 3 months of LARS implantation. The tunnels are marked with dashed yellow lines.

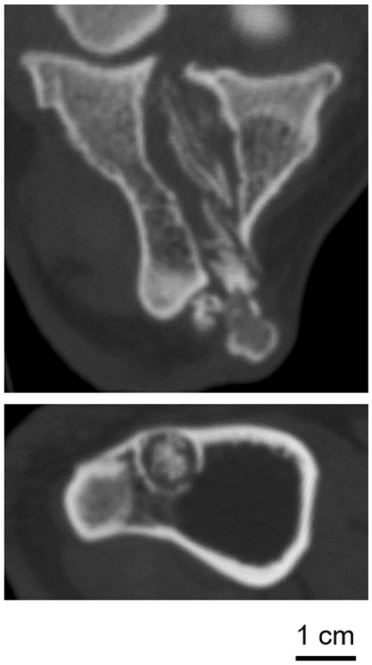

Supplementary Fig. 24 | CT images of femoral tunnel scanned in a coronal plane (top) and tibial tunnel scanned in an axial plane (bottom) after implanting HHF in sheep for 21 months.

Supplementary Table 1 | Mechanical performance of state-of-art materials for artificial and semitendinosus grafts.

Type	PET fibre	Carbon fibre	LARS	Autograft	HHF
Density (g/cm^3)	1.36	2.10	/	1.6	**0.478**
Young's modulus (GPa)	0.45-0.64	2.0-2.9	0.4-0.9	0.2-0.6	**0.472±0.12**
Stiffness (N/mm)	63.98±4.81	224.76±41.57	~89	17-106.5	**79.43±7.46**
Specific strength (N/tex)	0.12-0.15	0.07-0.10	0.04-0.06	0.02-0.06	**0.587±0.142**
Elongation (%)	41-53	11-17	8-10	13.0-86.1	**87.1±28.9**

The performances of autografts at **Supplementary Table 1** are cited from ref. *S13-16* and those for PET fibre and carbon fibre were tested.

Supplementary Table 2 | Bone repair performance of state-of-art materials for artificial ligaments.

Type	PET fibre	Carbon fibre	Autograft	HHF
BV/TV	0.08-0.19 (13 W)	0.05-0.21 (4 W)	0.20-0.30 (12 W)	**0.33-0.48 (13 W)**
Maximal pull-out force (N)	151.2±17.8 (13 W)	56.2±10.6 (13 W)	27.64±5.56 (16 W)	**207.5±21.5 (13 W)**
Healing of bone defect [#]	–52.1% (13 W)	Rupture (13 W)	-12.1% (16 W)	**+41.9% (13 W)**
Osteogenesis-related signaling pathways	WNT	WNT, MAPK	/	**WNT, MAPK, TGF-β**

[#]Healing of bone defect refers to the tunnel diameter change over 13 weeks, where "+" and "–" represent tunnel recovery and enlargement, respectively. The performances of autografts at **Supplementary Table 2** are cited from ref. *S13-17* and those for PET and carbon fibre were tested.

Caption for Supplementary Movie

Supplementary Movie 1 | Movement of a rabbit with reconstructed ACL using HHF graft on the hindlimb.

Supplementary Movie 2 | Movement of a control rabbit with torn ACL in the hindlimb.

Supplementary Movie 3 | Movement of a sheep with reconstructed ACL using HHF graft after 13 weeks of implantation.

Supplementary Movie 4 | Movement of a sheep with reconstructed ACL using HHF graft after 9 months of implantation.

Caption for Supplementary Data

Supplementary Data 1 | Differentially expressed proteins related to osteogenesis of MSCs cultured on HHF and helical PET fibres for the four timepoints, related to **Fig. 4b**.

Supplementary Data 2 | Differentially expressed proteins related to osteogenesis of MSCs cultured on PET plate, helical PET fibre, helical carbon fibre and HHF, related to **Fig. 4f**.

Supplementary Data 3 | Differentially expressed genes related to osteogenesis of MSCs cultured on PET plate, helical PET fibre, helical carbon fibre and HHF, related to **Extended Data Fig. 8d-f**.

Supplementary Data 4 | Differentially expressed proteins obtained from rabbit bone implanted with HHF and helical PET fibre for 2 weeks, related to **Fig. 4j**.

Supplementary Data 5 | Differentially expressed proteins related to osteogenesis of MSCs cultured on carbon plate, helical carbon fibre and HHF, related to **Supplementary Fig. 18**.

Supplementary Data 6 | Differentially expressed proteins related to osteogenesis of MSCs cultured on PET plate, helical PET fibre and hierarchical helical PET fibre, related to **Supplementary Fig. 19**.

Supplementary Data 7 | Differentially expressed proteins related to osteogenesis of MSCs cultured on HHF and hierarchical helical PET fibre, related to **Supplementary Fig. 20**.

Supplementary References

S1 Wang, Z. *et al.* Functional regeneration of tendons using scaffolds with physical anisotropy engineered via microarchitectural manipulation. *Sci. Adv.* **4**, eaat4537 (2018).

S2 Li, H. G. *et al.* Functional regeneration of ligament-bone interface using a triphasic silk-based graft. *Biomaterials* **106**, 180-192 (2016).

S3 Aka, C. Basal. G. Mechanical and fatigue behaviour of artifcial ligaments (ALs). *J. Mech. Behav. Biomed. Mater.* **126**, 105063 (2022).

S4 Brennan, D. A. *et al.* Mechanical considerations for electrospun nanofibers in tendon and ligament repair. *Adv. Healthcare Mater.* **7**, 1701277 (2018).

S5 Grana. W. A. *et al.* An analysis of autograft fixation after anterior cruciate ligament reconstruction in a rabbit model. *Am. J. Sport. Med.* **22**, 344-351 (1994).

S6 Wang, L. Y. *et al.* Functionalized helical fibre bundles of carbon nanotubes as electrochemical sensors for long-term in vivo monitoring of multiple disease biomarkers. *Nat. Biomed. Eng.* **4**, 159-171 (2020).

S7 Cao, C. H. *et al.* Buckling initiation and displacement dependence in compression of vertically aligned carbon nanotube arrays. *Carbon* **49**, 3190-3199 (2011).

S8 Bai, Y. X. *et al.* Storage of mechanical energy based on carbon nanotubes with high energy density and power density. *Adv. Mater.* **31**, 1800680 (2019).

S9 Hou, J. et al. An amorphous peri‐implant ligament with combined osteointegration and energy‐dissipation. *Adv. Mater.* **33**, 2103727 (2021).

S10 Wang, X. Tempering force with mercy: An innovative peri-implant ligament with combined osteointegration and energy-dissipation. *Nano Res.* **15**, 4466-4467 (2022).

S11 Osman, A. *et al.* Health aspects, growth performance, and meat quality of rabbits receiving diets supplemented with lettuce fertilized with whey protein hydrolysate substituting nitrate. *Biomolecules* **11**, 835 (2021).

S12 Han, S. H. *et al.* Cross-species transmission of swine hepatitis E virus genotype 3 to rabbits. *Viruses* **12**, 53 (2020).

S13 Zhao, F. *et al.* A more flattened bone tunnel has a positive effect on tendon-bone healing in the early period after ACL reconstruction. *Knee Surg. Sport. Tr. A.* **27**, 3543-3551 (2019).

S14 Brennan, D. A. *et al.* Mechanical considerations for electrospun nanofibers in tendon and ligament repair. *Adv. Healthcare Mater.* **7**, 1701277 (2018).

S15 Sugita, T., & A. A. Amis. Anatomic and biomechanical study of the lateral collateral and popliteofibular ligaments. *Am. J. Sport. Med.* **29**, 466-472 (2001).

S16 Aka, C. Basal. G. Mechanical and fatigue behaviour of artifcial ligaments (ALs). *J. Mech. Behav. Biomed. Mater.* **126**, 105063 (2022).

S17 Fanggang, et al. Anterior Cruciate Ligament Reconstruction in a Rabbit Model Using Silk-Collagen Scaffold and Comparison with Autograft. *PLOS ONE*. **10**, e0125900 (2015).